In-situ formation of carbon-doped cerium-zirconium solid solution as a superacid catalyst for the removal of NO$_x$

Ruihua Wang [a,1], Zhifei Hao [b,1], Xu Huang [b], Yue Peng [c,*], Guoquan Liu [a], Yuguo Xia [d], Sihui Zhan [a,*]

[a] *MOE Key Laboratory of Pollution Processes and Environmental Criteria, Tianjin Key Laboratory of Environmental Remediation and Pollution Control, College of Environmental Science and Engineering, Nankai University, Tianjin 300350, China*
[b] *College of Chemical Engineering, Inner Mongolia University of Technology, Hohhot 010051, China*
[c] *State Key Joint Laboratory of Environment Simulation and Pollution Control, National Engineering Laboratory for Multi Flue Gas Pollution Control Technology and Equipment, School of Environment, Tsinghua University, Beijing 100084, China*
[d] *School of Chemistry & Chemical Engineering, National Engineering Research Center for Colloidal Materials, Shandong University, Jinan 250100, China*

ARTICLE INFO

ABSTRACT

Defects engineering in nanomaterials can be used to precisely and effectively modulate catalysts' reactivity. Here we report a highly efficient NH$_3$-SCR catalyst constructed with *in-situ* formation of carbon-doped CeZrO$_{2-x}$ with dual defects, in which O atoms are substituted by C atoms to generate surface oxygen vacancies and subsurface oxygen substitutions. The carbon-doped CeZrO$_{2-x}$ exhibit superior activity and better SO$_2$/H$_2$O resistance compared with traditional bulk CeZrO$_x$ and V$_2$O$_5$-WO$_3$/TiO$_2$. The related characterization results reveal that the surface oxygen vacancy and subsurface oxygen substitution resulted in the formation of a large number of unsaturated coordination Ce and Zr species on catalyst's surface, which contributed to the adsorption and activation of NH$_3$, thus promoting the catalytic activity. Meanwhile, the abundant oxygen vacancy also stimulated the E-R reaction pathway over carbon-doped CeZrO$_{2-x}$. In addition, it was proved that more zirconium sulfate and unstable ammonium sulfate species were exposed over carbon-doped CeZrO$_{2-x}$, benifiting the better SO$_2$-tolerance.

1. Introduction

Defects engineering in nanomaterials has been proven as a feasible approach to manipulate their performance in catalytic field. [1–4] Oxygen vacancy, as a common crystal defect, results from the loss of lattice oxygen, exerting positive effects in elimination of pollutants. [5,6] As well known, ceria (CeO$_2$) is a kind of rich-vacancy metal oxide, in which the formation of oxygen vacancy can be expressed as: $O_o^x + 2Ce_{Ce}^x \rightarrow V_o^{\cdot\cdot} + 2Ce_{Ce}^{'} + 1/2\ O_2$. [7] Usually, it is recognized that there is a close relationship between oxygen vacancy and oxygen storage capability for ceria. In detail, the oxygen defects on CeO$_2$ surface can extract an O atom from a molecule to lead to reduction of the molecule. Meanwhile, CeO$_2$ can also oxidise a molecule by furnishing O atoms with reduction of the surface. In general, reactor stream conditions will decided the occurrence of oxidation or reduction. [7,8] Based on the above-mentioned characteristics, ceria-based catalysts are widely

concerned as a substitute of V$_2$O$_5$-WO$_3$/TiO$_2$ catalysts with the narrow activity window, the toxicity of active component vanadium and low SO$_2$ resistance in the removal of NO$_x$. [9–12] In general, due to poor thermal stability and surface acidity of pristine CeO$_2$, the Zr element is frequently doped into ceria-containing materials as structural promoter. [13,14] The introduction of Zr can regulate the valence states, defect sites and acidity of CeO$_2$, thus improving the activity of catalyst. [15] However, due to the poor uniformity of cerium zirconium oxides prepared by many traditional methods, [15] resulting in relatively less surface acidity and oxygen vacancy. On this basis, highly homogeneous Ce-Zr catalysts are worth designing to improve the surface acidity and defects of catalysts, thus improving the catalytic performance of NH$_3$-SCR at low temperature.

The metal-organic frameworks (MOFs) materials own high specific surface area, abundant pores and highly dispersed metal sites, and are often used as the support of highly dispersed active materials in the

---

process of catalyst preparation. [16–18] It has been reported that MOFs supported metal oxides catalysts has been successfully applied to the elimination of NO_x, and exhibited good catalytic performance. [19,20] Recently, a feasible strategy was developed for electronic structure modification of catalysts with doping-induced oxygen vacancy to boost catalytic performance, the simultaneous promotion of charge transfer and CO_2 activation over two-dimensional (2D) WO_3 nanosheets was achieved by coupling surface C-doping and oxygen vacancy. [21] Inspired by these facts, we attempted to use UiO-66 as support, a Zr-containing metal-organic framework (MOFs) with highly dispersed metal sites and well-defined defect sites, and supported cerium species to get the superacid carbon-doped Ce-Zr catalyst for the selective catalytic reduction of NO with NH_3 (NH_3-SCR) at low temperature.

In this work, combining the advantages of the defect-matrix in UiO-66 and superior redox ability of CeO_2, we demonstrate a facile pyrolysis strategy to synthesize carbon-doped $CeZrO_x$ (C-CZO_v) catalyst with surface oxygen vacancies and subsurface oxygen substitutions, which is used to probe the synergistic roles of dual defects on enhancement of sulfur resistance and low temperature catalytic activity for NH_3-SCR. Combined with the results of multiple spectroscopic analysis and theoretical simulations, it is shown that: i) O substitutions located in the C-CZO_v bulk phase can enhance the electron interaction between Ce and Zr species effectively, thus increase the Lewis acid sites; ii) O vacancies mainly located on the C-CZO_v surface can provide coordinatively unsaturated sites to induce strong interactions with NH_3, NO and O_2, promoting chemisorption and activation of reactant molecule. Notably, this design can also further improve the stability and surface acidity of the catalyst, i.e. the highly exposed Zr atoms on the catalyst surface can combine with SO_2 (when SO_2 is present in the feedgas) to protect the active component cerium, and the resulting zirconium sulfate can provide a new acid site for the reaction.

2. Experimental section

2.1. Catalyst preparation

All the reagents are commercially available and used as received if without special explanation.

A classical solvothermal method was employed to synthesize the precursor UiO-66. First, 1.06 g $ZrCl_4$, 0.68 g p-phthalic acid and 6 ml acetic acid were successively dispersed in 76 ml DMF solvent by sustained sonication for 30 min to obtain a homogeneous solution. Then, the preparatory solution was transferred into a Teflon-sealed autoclave and heat at 120 °C for 24 h. When cooled to room temperature, the synthetic white precipitates (UiO-66) were washed with ethanol for several times. Finally, the UiO-66 was dried in a vacuum oven at 200 °C for 8 h.

Synthesis of the carbon-doped $CeZrO_{2-x}$: At first, 1 g UiO-66 were dispersed in 40 ml ethanol solution containing a certain amount of Ce $(NO_3)_3·6 H_2O$ with sustained sonication for 10 min, and then stirred for 4 h to obtain a homogeneous suspension. Next, the suspension was stirred at a water bath temperature of 70 °C until ethanol disappeared completely. In the final, samples were calcined at 800 °C for 3 h in Ar atmosphere to obtain the carbon-doped $CeZrO_{2-x}$ catalyst. A series of ratio (the mass ratio of cerium to UiO-66) were set up as 0.15, 0.20, 0.25 and 0.35, which are named C-C_xZO_v (x = 0.15, 0.20, 0.25 and 0.35), in which x represents the mass ratio of cerium to UiO-66, v represents the oxygen vacancy, and C-$C_{0.25}ZO_v$ was selected as the representative sample for further study due to the best catalytic properties (Fig. S5, unless otherwise noted, C-CZO_v in subsequent chapters refers to C-$C_{0.25}ZO_v$). Meanwhile, the pure carbon-doped ZrO_2 (denoted as C-ZrO_2) was prepared as comparison under the same condition without cerium nitrate.

Synthesis of $CeZrO_x$: X-ray fluorescence analysis (Table S1) demonstrated that the molar ratio of Ce/Zr in C-CZO_v was exactly 1:1. Refer to this ratio, Ce$(NO_3)_3·6 H_2O$ and $ZrCl_4$ were dissolved in 40 ml ethanol

and stirred for 4 h. After drying the mixed solution, the mixture solid was calcined in the atmosphere of air (muffle furnace) at 500 °C for 4 h to form the $CeZrO_x$ sample (labeled as CZO). CeO_2 was synthesized after undergoing same process without zirconium chloride.

Synthesis of V_2O_5-WO_3/TiO_2 sample: At first, NH_4VO_3 and $(NH_4)_{10}W_{12}O_{41}·xH_2O$ were dissolved in deionized water, complexing with oxalic acid at the same time. After that, support TiO_2 was introduced into the above solution, stirring for 2 h at room temperature. Excess water was evaporated by a magnetic stirring apparatus. The sample could be obtained after a drying (100 °C for 12 h) and calcining (muffle furnace, 500 °C for 5 h, air atmosphere) process (labeled as V-W/TiO_2, the powder XRD patterns of V-W/TiO_2 is showed in Fig. S1).

2.2. Catalyst characterization

The details of the catalyst characterization and DFT calculation are described in Supporting Information.

2.3. Catalytic activity tests

Activity tests were carried out in a fixed-bed quartz reactor with the inner diameter of 5 mm. Prior to each test, 0.1 g 40–60 mesh catalyst was used. The feed gas included 500 ppm NO, 500 ppm NH_3, 5% O_2, 5 vol% H_2O (when used), 100 ppm SO_2 (when used) and N_2 as balance. The total flow rate of the feed gas was 200 ml min^{-1} and the gas hourly space velocity (GHSV) was approximately 60, 000 ml g^{-1} h^{-1}. The concentrations of the gases (NO, NO_2, N_2O, and NH_3) were continually monitored by an FTIR spectrometer (MultiGas TM 2030 FTIR Continuous Gas Analyzer). The concentration data were collected when the reaction reached a steady state after 30 min at each temperature. The NO_x conversion rate and N_2 selectivity were defined by the following equations:

$$NO_x \text{ conversion } (\%) = 100\% \times \frac{[NO_x]_{in} - [NO_x]_{out}}{[NO_x]_{in}}$$

$$N_2 \text{ selectivity } (\%) = 100\%$$
$$\times (1 - \frac{2[N_2O]_{out}}{[NH_3]_{in} + [NO_x]_{in} - [NH_3]_{out} - [NO_x]_{out}})$$

The $[NO_x]_{in}$ and $[NO_x]_{out}$ noted the inlet and outlet concentration at steady-state, separately ($[NO_x] = [NO] + [NO_2]$).

3. Results and discussion

3.1. Synthesis and microstructure of carbon-doped $CeZrO_{2-x}$

In this study, UiO-66, a Zr-containing metal organic frameworks (MOFs), was chosen as the model system owning to the highly dispersed metal sites and well-defined defect sites (Fig. S2-S4). [22] The carbon-doped $CeZrO_{2-x}$ catalyst with dual defects were synthesized by a facile pyrolysis of UiO-66 supported cerium species, in which O atoms were substituted by C atoms to generate surface oxygen vacancies and subsurface oxygen substitutions. The preparation process and proposed formation mechanism are shown in Fig. 1a.

The microstructure and composition of as-prepared samples were first characterized by X-ray diffraction (XRD) and Transmission electron microscopy (TEM). As shown in Fig. 1b, the calcined pure UiO-66 mainly presents the cubic phase of ZrO_2 (JCPDS:49–1642) with the space group Fm-3 m after calcination at 800 °C in Ar atmosphere (C-ZrO_2), the diffraction peaks at 30.1 and 50.2° corresponding to the (111) and (220) crystal planes. [20] After the introduction of Ce species, it was observed that the diffraction peak of (111) and (220) of C-CZO_v shifted towards to the low diffraction angle, which were exactly between the diffraction peaks of pure cubic CeO_2 (JCPDS:34–0394) and C-ZrO_2, indicating that Ce-O-Zr structure may be formed during the preparation
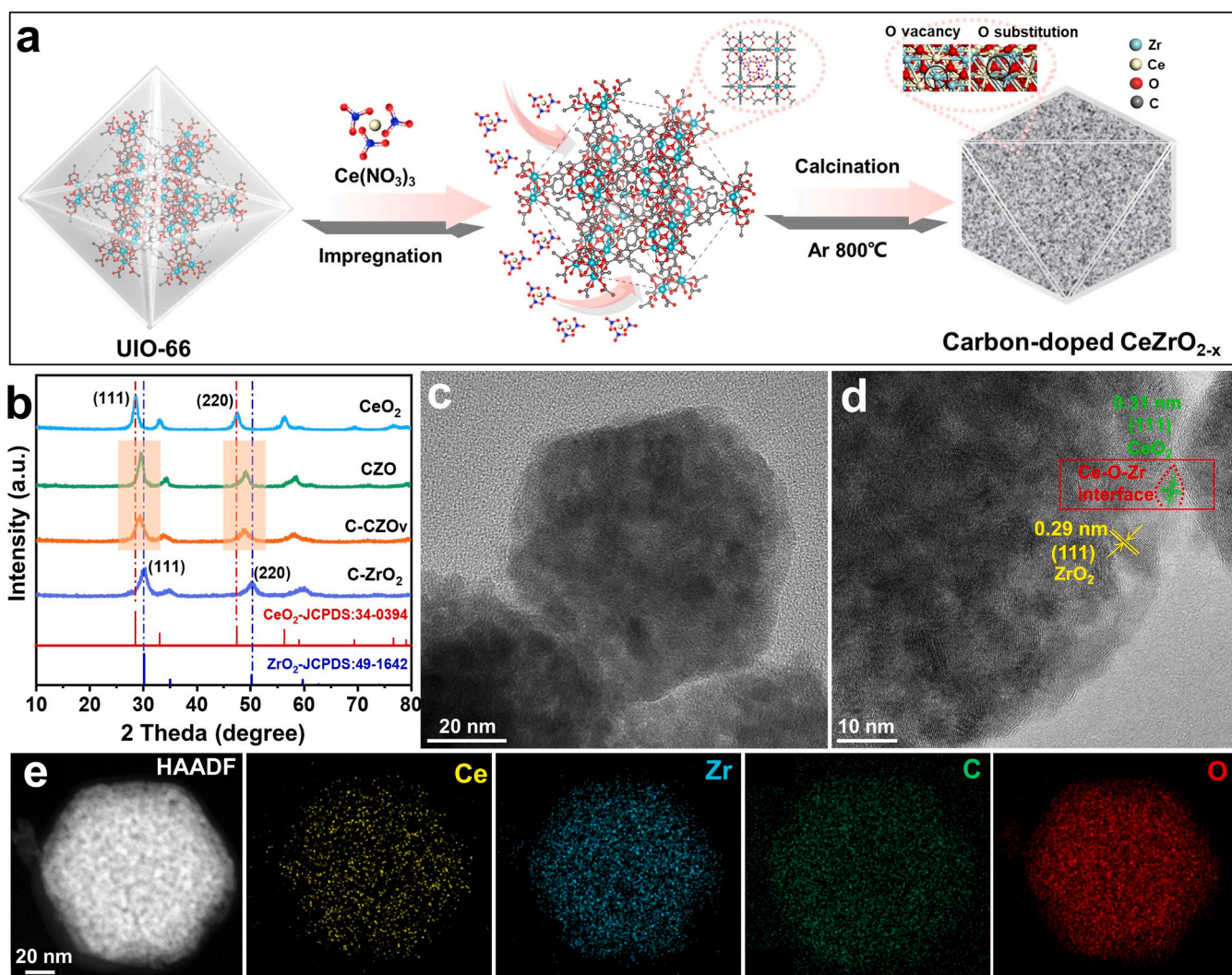
Fig. 1. (a) Schematic illustration for the synthesis of carbon-doped CeZrO$_{2-x}$. (b) The powder XRD patterns of CeO$_2$, CZO, C-CZO$_v$, C-ZrO$_2$. (c-e) HRTEM images of C-CZO$_v$ and EDXS-Mapping analysis of C-CZO$_v$.

process. Similarly, the same phenomenon was observed in the CZO, but the full-width of half maximum (FWHM) of the diffraction peak of C-CZO$_v$ was much wider than CZO, indicating that the crystallinity of C-CZO$_v$ was reduced, which may be caused by the defects formed by C doping. Then the transmission electron microscopy (TEM) was employed to explore the crystal structure and dispersion of Ce and Zr species in C-CZO$_v$. The C-CZO$_v$ and C-ZrO$_2$ mainly show distorted octahedral morphology, which is evolved from the octahedral shape of UiO-66 (Fig. 1c and S6). However, it is worth noting that there exists obvious aggregation of fine black carbon particles on the surface of C-ZrO$_2$ from the carbonization of UiO-66 during high temperature calcination, while no obvious carbon particles were observed on the surface of C-CZO$_v$, indicating C atoms of C-CZO$_v$ exist in doped form or some of the C atoms are volatilized during pyrolysis. The high-resolution TEM (HRTEM) image (Fig. 1d) reveals the 0.29 nm and 0.31 nm interplanar distances are assigned to the d$_{(111)}$ spacing of ZrO$_2$ and CeO$_2$ respectively. [23] In particular, a representative HRTEM image of CeO$_2$-ZrO$_2$ at the interface shows distinct contrast and dissimilar lattice fringes of CeO$_2$ and ZrO$_2$, indicating the existence of Ce-O-Zr structure at interface. Furthermore, the TEM-energy dispersive X-ray spectroscopy (EDXS) mapping images confirm that the C, Ce, O and Zr elements are homogeneously distributed over C-CZO$_v$ (Fig. 1e).

3.2. Insight into the dual-defect of carbon-doped CeZrO$_{2-x}$

To ascertain the existence form of the doped C and location of O substitutions in the C-CZO$_v$, elemental analysis and Raman spectroscopy were employed. As shown in Table S1, the atomic percentage ratio of Ce and Zr in the C-CZO$_v$ is close to 1, but the contents of C and O are significantly different between C-ZrO$_2$ and C-CZO$_v$ (Table S2), whereas the ratio of O to C in C-CZO$_v$ show a significant decrease, indicating that there is less O content in C-CZO$_v$ and there may be more oxygen vacancies on its surface. This can also be confirmed by the Raman spectroscopy (Fig. 2a), except for the similar characteristic peaks of ZrO$_2$ (246, 304, 455, 630 cm^{-1}) and CeO$_2$ (465, 595 cm^{-1}), [23] both the C-CZO$_v$ and C-ZrO$_2$ show the D (1354 cm^{-1}) and G (1599 cm^{-1}) bands of graphitic carbon, but the intensity of I$_D$/I$_G$ in C-CZO$_v$ is much lower than that in CZO, indicating C atoms exist mainly in doped form. [24] Thus, it is more likely that O atoms are substituted by C atoms, rather than that Zr or Ce atoms are substituted or C atoms stay at the interstitial sites.

To experimentally identify the above results, oxygen temperature-programmed desorption (O$_2$-TPD) and electron paramagnetic resonance (EPR) are performed, referenced against CZO. As shown in Fig. 2b, two desorption peaks of O$_2$ concentrated at 130 °C and 530 °C were observed at C-CZO$_v$, corresponding to the chemisorption oxygen and lattice oxygen respectively, [25,26] As for the CZO, the desorption
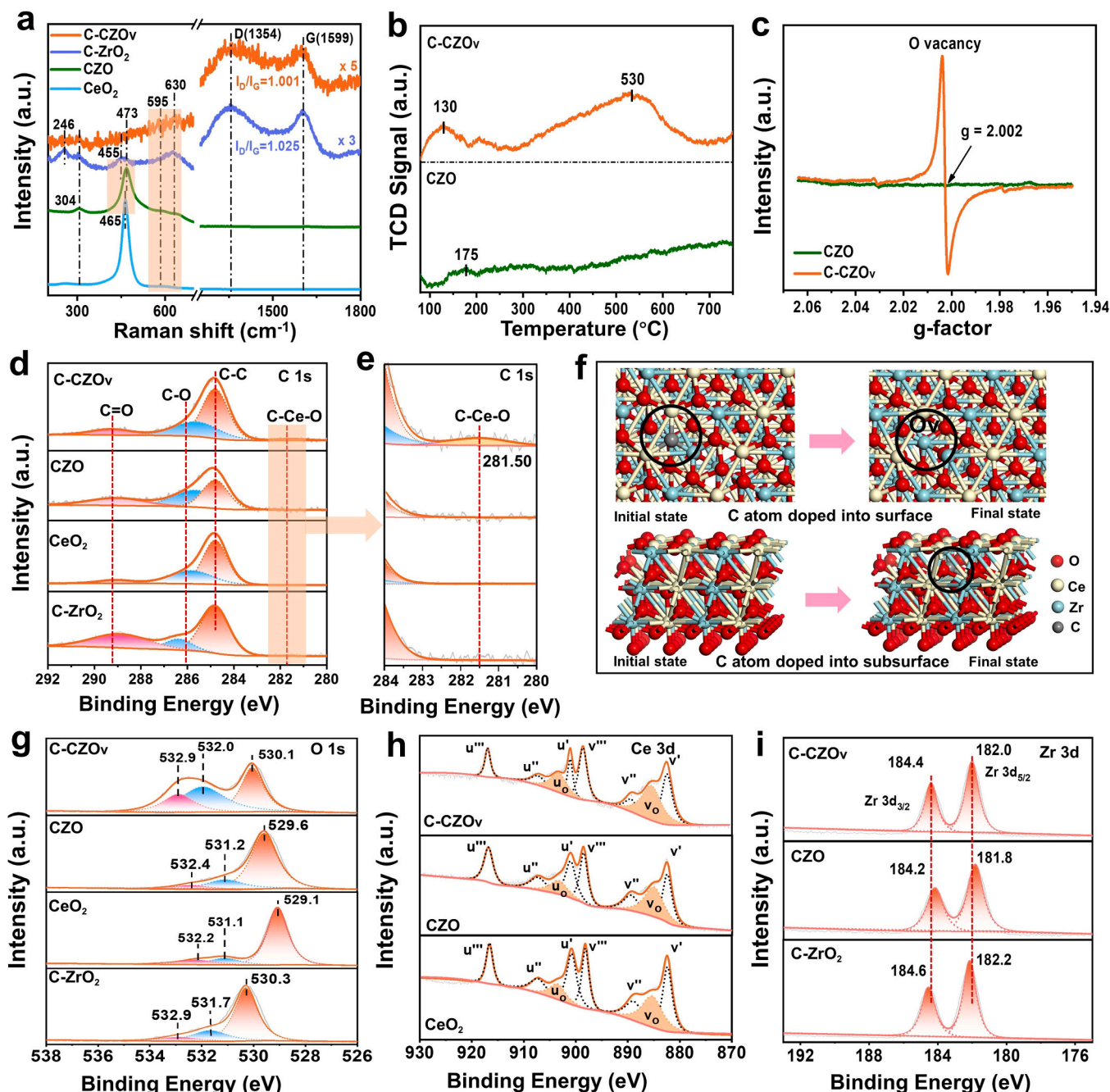
Fig. 2. (a) The Raman spectroscopy of CeO$_2$, CZO, C-ZrO$_2$, C-CZO$_v$. (b) O$_2$-TPD profiles of CZO, C-CZO$_v$. (c) EPR spectra of CZO, C-CZO$_v$. (d-e) XPS spectra of C 1 s (f) Structure optimization of surface and subsurface C doping. (g-i) XPS spectra of O 1 s, Ce 3d and Zr 3d.

peak of O$_2$ intensity is very weak, indicating that its adsorption capacity for O$_2$ is relatively weak. This result can also be proved directly by EPR (Fig. 2c), as compared with CZO, the C-CZO$_v$ exhibits a significant signal at g= 2.002, which can be attributed to the electrons trapping at oxygen vacancies. [27,28] O$_2$-TPD and EPR spectroscopy give information about both the surface and the bulk, to further quantitatively estimate the surface O vacancy concentrations, we examined the samples by XPS. As shown in Fig. 2g, the peak of O 1 s was fitted into three sub-bands. The three sub-bands at 529.6–530.3 eV, 531.1–532.0 eV and 532.2–532.9 eV can be assigned to the lattice oxygen (marked as O$_\beta$), chemisorbed oxygen species such as hydroxyl-like groups or defect-oxide (denoted as O$_\alpha$) and chemisorbed water (denoted as O$_\alpha$'), separately. [29] It is obvious that there were more chemisorbed oxygen species in C-CZO$_v$ and the corresponding O$_\alpha$/O$_\beta$ ratio was about five

times than that of CZO (Table S3). Meanwhile, from the XPS spectra analysis of Ce 3d (Fig. 2h and Table S3), the C-CZO$_v$ also exhibited the highest content of Ce^{3+}, indicating the presence of numerous oxygen vacancies. Moreover, it is known that the presence of vacancies and substitutions can strongly affect the electronic states of chemical bonds of materials, thus the XPS spectra of Zr 3d in C-CZO$_v$ shift to lower binding energy compared with the C-ZrO$_2$ (Fig. 2i), which can be induced by more O vacancies and O substitutions.

To further resolve the status of doped C, we also collected C 1 s XPS spectra (Fig. 2d-e). All the samples indicated the presence of C-C (284.6 eV), C-O (286.05 eV) and C=O (288.4 eV) structure. [30] Notably, C-CZO$_V$ showed another peak at 281.50 eV, which corresponds to the C–Ce-O coordination, [31] thus further suggesting that C atoms substitute O atoms. Furthermore, the formation mechanism of O

vacancy and O substitution were investigated by the DFT calculations. As shown in Fig. 2f, when C atoms are doped into the surface of $Ce_{0.5}Zr_{0.5}O_2$ (111) by substituting surface O atoms, C atom is unstable and tend to form CO with the nearby O atom, which then desorbs to form surface oxygen vacancy. The oxygen vacancy formation energy is -4.67 eV, indicating that the process is feasible in energy principle. We also calculate the process of C doping into the subsurface (Fig. 2f), one subsurface O atom is substituted with one C atom on the subsurface of $Ce_{0.5}Zr_{0.5}O_2$ (111), the formation energy is -3.25 eV, thus implying that the doped C is only stably located in the subsurface.

3.3. NH3-SCR activity of carbon-doped CeZrO2−x

Fig. S5 shows the NH3-SCR performance as a function of temperature over the carbon-doped CeZrO2−x, by comparing the catalytic activity of the samples loaded with different rations of Ce species, we confirm the optimal loading amount of Ce species is 0.25 wt%, in which NOx conversion can achieve 54.1% at 200 °C and keep higher than 85% from 250 to 400 °C. Meanwhile, the catalytic activity of C-CZOv was also compared to the commercial V_2O_5-WO_3/TiO_2 [32] and CZO. As shown in Fig. 3a, the C-CZOv showed a much higher activity advantage at low temperature with a wide-operating temperature window. Besides, C-CZOv catalyst also exhibit superior N2 selectivity in the whole temperature range (Fig. S7). A slight decrease of N2 selectivity occurred above 300 °C for C-CZOv and CZO, which was related to the oxidation of ammonia at high temperature. [33] Thus, the excellent catalytic activity of the C-CZOv catalyst was due to the strong interaction between carrier UiO-66 and Ce species. To further reveal the reasons for the performance

improvement of NH3-SCR, we choose C-CZOv and CZO for detailed study.

Sulfur dioxide (SO2) and water vapor (H2O) usually accompany with the combustion exhaust, which were considered to be two key causes of inactivation of NH3-SCR catalysts. Therefore, the tolerance tests of SO2 (100 ppm) and H2O (5 vol% H2O) over C-CZOv and CZO were carried out. As shown in the Fig. 3b, it is noteworthy that after the introduction of SO2 at 300 °C, the NOx conversion of C-CZOv and CZO increased from 98.3% and 70.1% of the initial reaction state to 100% and 86.3%, respectively. Meanwhile, the N2 selectivity of C-CZOv and CZO were also increased to 100%. This may be due to the formation of metal sulfates on the catalyst surface during the reaction. On the one hand, the presence of metal sulfate forms a new acid site, which can improve the conversion rate of NOx. On the other hand, metal sulfuric acid inhibits the collision between adsorbed ammonia and high oxidized metal ions, resulting in less ammonia oxidation, which was beneficial to the better selectivity of N2. [34] After this, due to the continuous accumulation of sulfates on the catalyst surface, deNOx activity of both catalysts began to decline and then stabilized. It was noted that the C-CZOv showed better SO2-tolerance than CZO, the NOx conversion rate decreased by 6.6% and 14.4% from initial peak to steady state, respectively. When SO2 and H2O were simultaneously introduced into the feed gas (Fig. 3c), the NOx conversion rate of CZO decreased by 23.0% compared with the initial peak, while the NOx conversion rate of C-CZOv decreased by only 14.6%. The overall trend of N2 selectivity and NOx conversion was the same as when SO2 was introduced only in the Figs. 4b and 5. These results demonstrated that the C-CZOv possessed a good SO2/H2O resistance. Besides, C-CZOv and CZO exhibited excellent thermal stability (Fig. 3d, S8 and

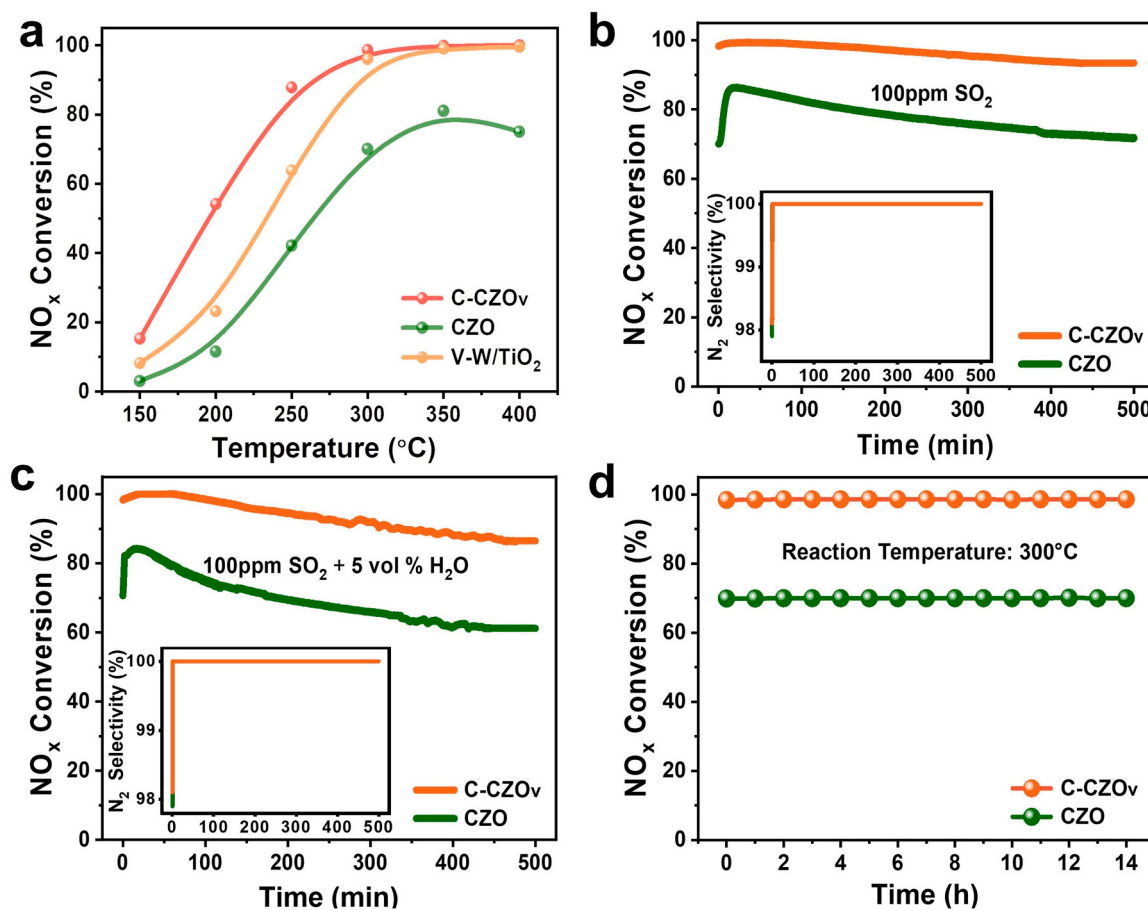**Fig. 3.** (a) NOx conversion of C-CZOv, CZO and V-W/TiO2. (b-c) Resistance tests of C-CZOv and CZO: 100 ppm SO2 resistance (b), 5 vol% H2O + 100 ppm SO2 resistance (c). (d) stability tests of C-CZOv and CZO. Reaction conditions: [NO] = [NH3] = 500 ppm, [O2] = 5 vol%, [SO2] = 100 ppm (when used), [H2O] = 5 vol% (when used), reaction temperature at 300 °C (b, c, d), GHSV = 60, 000 ml g^{-1} h^{-1} and N2 as balance.

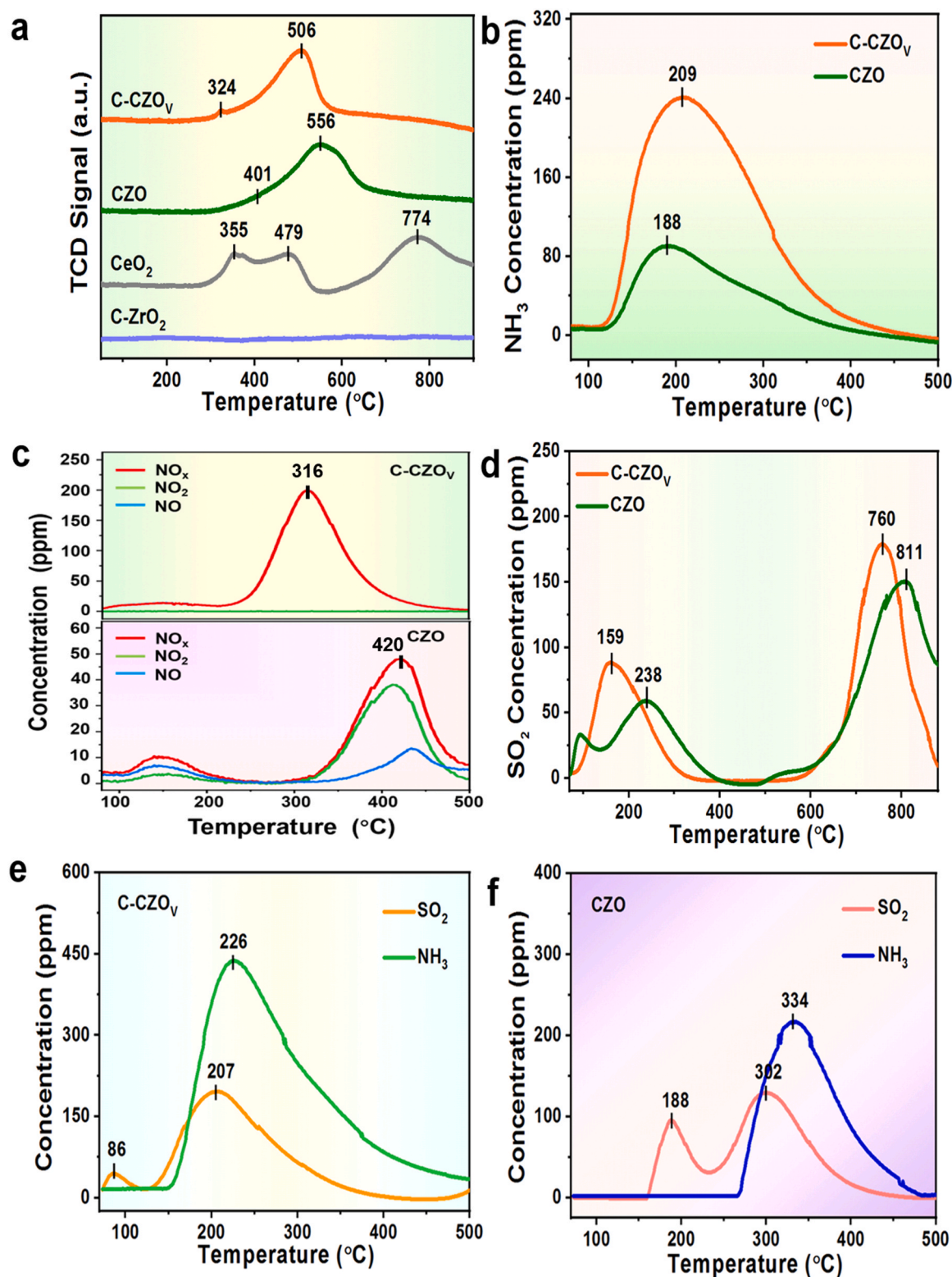**Fig. 4.** (a) H_2-TPR profiles of CeO_2, CZO, C-ZrO_2 and C-CZO_v. (b) NH_3-TPD profiles of CZO and C-CZO_v. (c) NO+O_2-TPD profiles of CZO and C-CZO_v. (d) The SO_2 +O_2-TPD profiles of C-CZO_v and CZO. (e -f) The NH_3 +O_2 +SO_2-TPD profiles of C-CZO_v (e) and CZO (f).

S9), and all peaks of the XRD patterns of fresh C-CZO_v and CZO (Fig. S10 and Fig. S11) are consistent with the used C-CZO_v and CZO, demonstrating that the microstructure of catalysts remain unchanged before and after reaction. Based on the above experimental results and discussion, the calcined UiO-66 support with special structure protected the Ce/Zr active components from the SO_2 and H_2O. Compared with the

CZO, C-CZO_v showed the excellent catalytic activity and had a potential application prospect.

3.4. Surface reducibility and adsorption behavior of NH_3/NO+O_2/SO_2

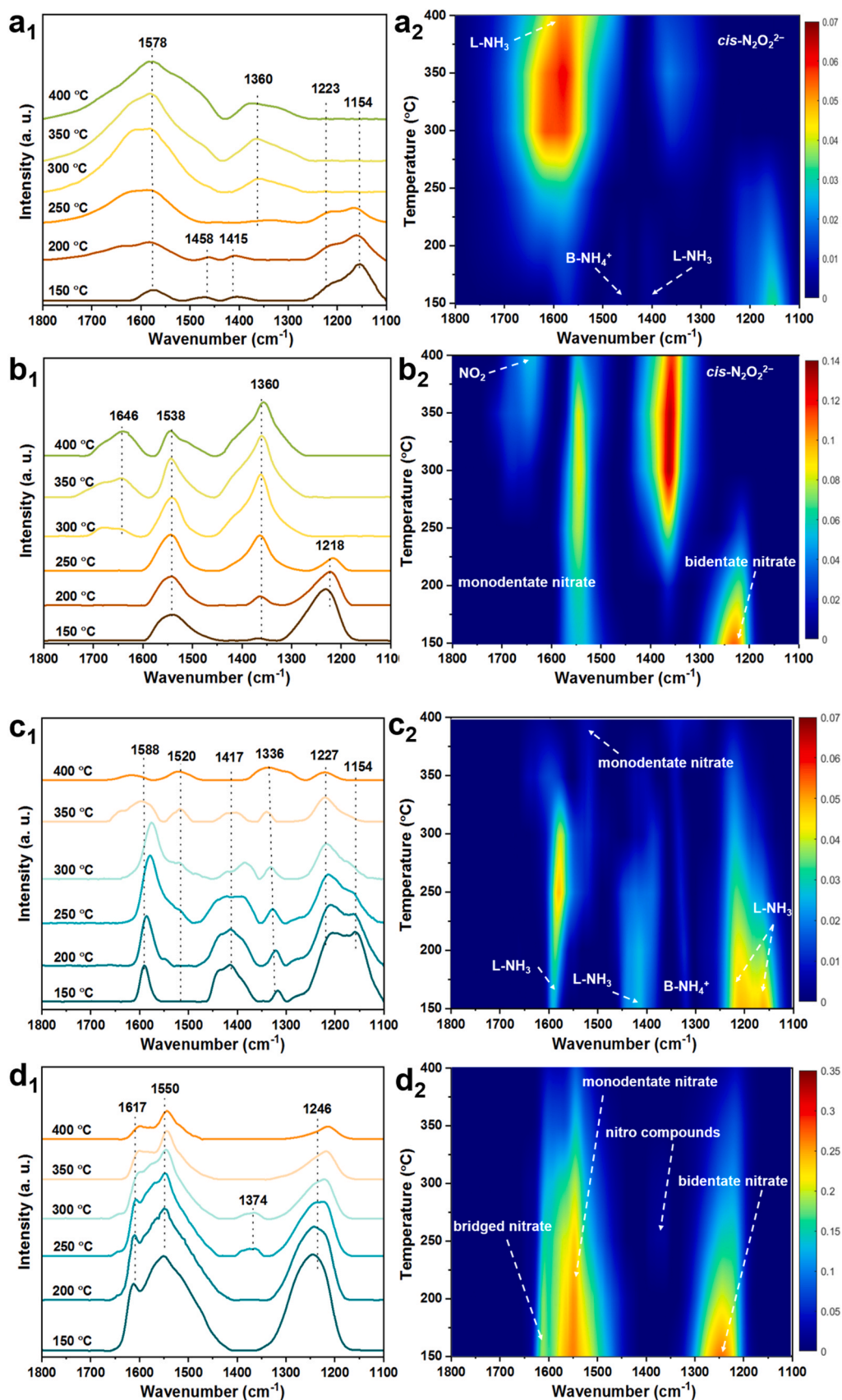To directly evaluate the redox properties of the catalyst, the

Fig. 5. In situ DRIFTS spectra of NH₃ adsorption over C-CZOᵥ (a₁, a₂)and CZO (c₁, c₂) and NO adsorption over C-CZOᵥ (b₁, b₂) and CZO (d₁, d₂) in the temperature range of 150–400 °C, respectively.

hydrogen temperature-programmed reduction (H$_2$-TPR) experiment was performed and the corresponding result is shown in Fig. 4a. For the pure C-ZrO$_2$, there was no obvious peak in the calcined UiO-66, because the oxidation state of Zr is difficult to reduce at low temperature. [35] As for pure CeO$_2$, the peaks of at 355 °C, 479 °C and 774 °C could be related to the reduction of surface oxygen species, subsurface layers and bulk CeO$_2$ for pure CeO$_2$, respectively. [36] When the introduction of Ce species into the C-ZrO$_2$, TPR-curves changes dramatically, the H$_2$ consumption uptake at 506 °C and 556 °C in C-CZOv were assigned to the reduction of Ce^{4+} connected with Zr^{4+}, [36,37] the reduction peaks moved to lower temperature compared with CZO, indicting the enhancement of low temperature redox capability.

It is well known that the catalytic reaction originates from the adsorption of reactant molecules. Thus, a series of experiments were performed to test the catalysts adsorption capacity. At first, NH$_3$-TPD was employed to investigate distribution of acid sites over samples. As shown in Fig. 4b, single broad desorption peak spanned in the temperature range of 120–450 °C for both catalysts, which was assigned to NH$_3$ species desorbed by weak and medium acid sites. From the position and area of NH$_3$ desorption peak, it can be concluded that the C-CZO$_v$ is significantly superior to CZO on the strength and number of acid centers. Furthermore, it is noteworthy that more NO was generated for C-CZO$_v$ than CZO during the NH$_3$-TPD tests (Fig. S12), indicating that the NH$_3$ activation ability of C-CZO$_v$ was stronger. The relative reason is described as follows: the large amount of oxygen vacancies strengthened the electrophilicity of catalyst for C-CZO$_v$, which enhanced electronic transfer from NH$_3$ to metal atoms, leading to the N-H bond of NH$_3$ molecule more easily broken to combine with surface oxygen to generate NO.

NO+O$_2$-TPD over CZO and C-CZO$_v$ were also carried out. For the NO+O$_2$-TPD profiles in Fig. 4c, C-CZO$_v$ has a lager desorption amount of NO$_x$ than CZO, indicating the better NO$_x$ adsorption capacity. Moreover, the initial NO$_x$ desorption temperature of C-CZO$_v$ shifts to the lower temperature, which proves that more unstable nitrate presents on C-CZO$_v$. The formation of unstable nitrate is considered to be related to the doped carbon in C-CZO$_v$, which induced surface oxygen vacancies and subsurface oxygen substitutions causes the unsaturated coordination of cerium, resulting in the unstable binding of cerium to nitrate. [38] In addition, no NO$_2$ was released in the NO+O$_2$-TPD process of C-CZO$_v$, which could be ascribed to the reaction (CeO$_{2-x}$ + NO$_2$ → CeO$_2$ + NO) on the defective catalyst surface. [39]

In order to track the formation of sulfate species in test of SO$_2$-resistance, we performed SO$_2$ +O$_2$-TPD and NH$_3$ +SO$_2$ +O$_2$-TPD measurements on C-CZO$_v$ and CZO. As reported in Fig. 4d, the peaks below 400 °C and above 600 °C can be assigned to desorption of the weakly adsorbed SO$_2$ and metal sulfate, respectively. The desorption temperatures of C-CZO$_v$ (159 °C, 760 °C) are lower than CZO (238 °C, 811 °C), implying the less intense effects between SO$_2$ and C-CZO$_v$. In the Table S3, it can be concluded from the Ce^{3+}/Ce^{4+} ratio before and after SO$_2$-resistance experiments that more Ce^{4+} combined with SO$_2$ to form Ce(SO$_4$)$_2$ on C-CZO$_v$ surface than CZO. The Ce(SO$_4$)$_2$ is less stable than Ce$_2$(SO$_4$)$_3$, [11] which accounts for the lower-temperature decomposition of metal sulfate for C-CZO$_v$ in Fig. 4d. The NH$_3$ +SO$_2$ +O$_2$-TPD results of C-CZO$_v$ and CZO were displayed in Fig. 4e-f. The desorption peaks of SO$_2$ at 86 °C, 188 °C, 207 °C and 302 °C in Fig. 4e-f separately originated from physically adsorbed SO$_2$, chemically adsorbed SO$_2$ and ammonium sulfate. [11] It is found that the ammonium sulfate formed on CZO is more stable than that on C-CZO$_v$. The reason for this fact is that the doped carbon of C-CZO$_v$ segregated the direct connection between some ammonium sulfate and the surface metal atoms, inducing the poor thermal stability of ammonium sulfate. Moreover, the temperature (207 °C) of SO$_2$ desorption peak corresponding to ammonium sulfate was lower than reaction temperature (300 °C) in Fig. 4e, which means that much ammonium sulfate on C-CZO$_v$ could be decomposed to release active sites. It can be also clearly observed from Fig. 4e-f that C-CZO$_v$ had lager capacity for SO$_2$ adsorption, which is assigned to

generous oxygen vacancies in C-CZO$_v$. In addition, it's remarkable that the surface Ce/Zr ratio on C-CZO$_v$ was increased after SO$_2$-resistance test in the Table S3, while CZO presented the opposite trend. It indicates that more zirconium sulfate formed on C-CZO$_v$ during SO$_2$-resistance experiment, which not only protected the active component cerium, but also generated new acid sites for NH$_3$-SCR reaction. Overall, the less deactivation effect of C-CZO$_v$ for SO$_2$-resistance test can be attributed to the formation of unstable ammonium sulfate and more zirconium sulfate.

The *in situ* DRIFTS spectra of NH$_3$ adsorption were taken with the ramping temperature to detect the NH$_3$ adsorption behaviors over catalysts (Fig. 5a$_1$,a$_2$, c$_1$, c$_2$). The bands (1154 cm^{-1}, 1223 cm^{-1}, 1227 cm^{-1}, 1415 cm^{-1}, 1417 cm^{-1}, 1578 cm^{-1}, 1588 cm^{-1}) could be assigned to the NH$_3$ coordinated to the Lewis acid sites (L-acid). [40–42] While the features at 1336 cm^{-1} and 1458 cm^{-1} are ascribed to NH$_4^+$ bonded with Brønsted acid sites (B-acid). [34,43] It can be observed that L-acid sites are mainly in C-CZO$_v$, while CZO mainly contains two acid sites: B-acid sites and L-acid sites. Moreover, it is noticeable that the signal of NH$_3$ coordinated to the L-acid sites (1578 cm^{-1}) for C-CZO$_v$ could be maintained when temperature was above 300 °C, while all NH$_3$ absorption bands (1154 cm^{-1}, 1223 cm^{-1}, 1417 cm^{-1} and 1588 cm^{-1}) were weakened for CZO, indicating that the the L-acid sites on C-CZO$_v$ were stronger than these acid sites on CZO. This result also provides explanation for the higher desorption temperature of NH$_3$ (Fig. 4b) and wider operating temperature window (Fig. 3a) of C-CZO$_v$. In addition, some new bands of *cis*-N$_2$O$_2^{2-}$ (1360 cm^{-1}) and monodentate nitrate (1520 cm^{-1}) appeared with ramping temperature in Fig. 5a$_1$ and c$_1$, which were related to NH$_3$ oxidation at higher temperature. [44]

The *in situ* DRIFTS spectra obtained during NO+O$_2$ adsorption on catalysts are shown in Fig. 5b$_1$, b$_2$, d$_1$, d$_2$. Abundant N-containing species were observed, including gaseous NO$_2$ (1646 cm^{-1}), bridged nitrate (1617 cm^{-1}), monodentate nitrate (1538 cm^{-1} and 1550 cm^{-1}), nitro compounds (1374 cm^{-1}), *cis*-N$_2$O$_2^{2-}$ (1360 cm^{-1}), bidentate nitrate (1246 cm^{-1} and 1218 cm^{-1}). [11,34,43,44] Among these N-containing species, *cis*-N$_2$O$_2^{2-}$ species is attributed to the NO coordinated to oxygen vacancy. [1] With increasing temperature, the signal of bidentate nitrate over C-CZO$_v$ decreased and further vanished, and *cis*-N$_2$O$_2^{2-}$ species and gaseous NO$_2$ alternatively appeared and strengthened (Fig. 5b$_1$-b$_2$). Cheng et. al stated that bidentate nitrate could transform to monodentate nitrate, which would be further decomposed to NO$_2$. [45] Therefore, based on this fact and the changes of bands in Fig. 5b$_1$, we can make a reasonable inference on the NO$_x$ adsorption behaviors of C-CZO$_v$ at different temperatures as follows: (1) NO$_x$ was adsorbed on C-CZO$_v$ surface to form monodentate and bidentate nitrate at low temperature; (2) With elevated exposure temperature, bidentate nitrate gradually transformed to monodentate nitrate and NO$_2$; (3) The formed NO$_2$ was adsorbed on vacancy and then reduced to NO, and then NO continued to be linked with vacancy to generate *cis*-N$_2$O$_2^{2-}$ species. The *in situ* DRIFTS spectra of CZO when NO and O$_2$ entered in the reaction atmosphere was shown in Fig. 5d$_1$ and d$_2$, all band signals (except 1374 cm^{-1}) exhibited the downward trend with the increase of temperature, illustrating the decrease of adsorbed nitrate species. Moreover, appearance and disappearance of the feature at 1374 cm^{-1} were ascribed to the adsorption and desorption of NO$_x$ species, respectively. Compared with C-CZO$_v$, there is no adsorption of gaseous NO$_2$ and *cis*-N$_2$O$_2^{2-}$ species on CZO, indicating that the reduction of NO$_2$ to NO did not happen because of deficient vacancies. Sum up, the *in situ* DRIFTS spectra of NO+O$_2$ adsorption are in good agreement with NO+O$_2$-TPD results as well.

3.5. Reaction mechanism based on in situ DRIFTS

The *in situ* DRIFTS spectra over C-CZO$_v$ and CZO were measured to explore reactive intermediate species at 300 °C, the results were showed up in Fig. 6a$_1$, a$_2$,b$_1$, b$_2$. Fig. 6 a$_1$-a$_2$, shows that the pre-absorbed NH$_3$ linked to L-acid sites (1159, 1223 and 1605 cm^{-1}) vanished in 1 min after the addition of NO and O$_2$, indicating that coordinated NH$_3$ species
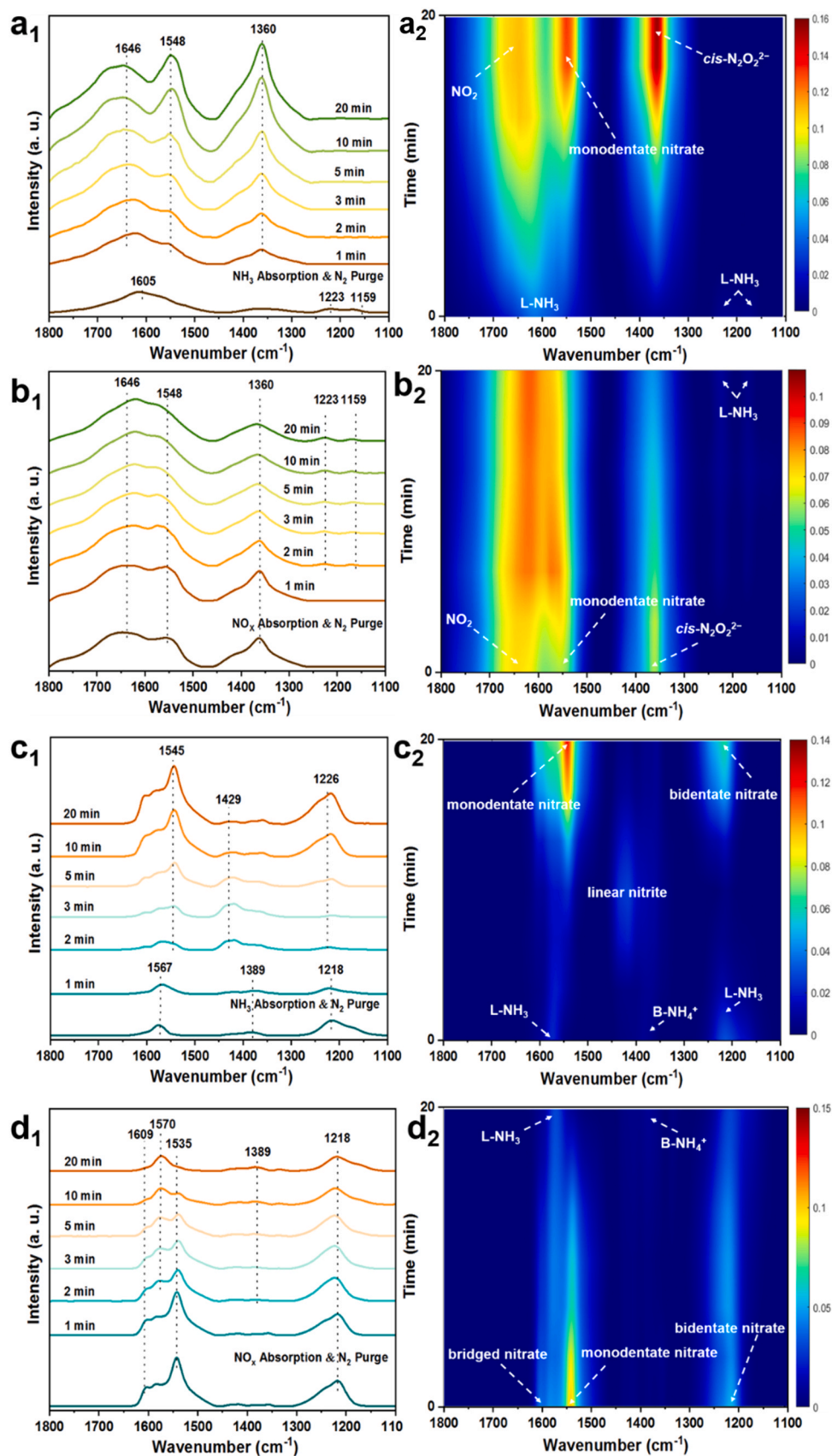
Fig. 6. In situ DRIFT spectra for the reactions between preadsorbed NH₃/NOx and NO+O₂/NH₃ over C-CZOᵥ (a₁, a₂, b₁, b₂) and CZO (c₁, c₂, d₁, d₂) at 300 °C.

on C-CZO$_v$ reacted with gaseous NO. Along with the reaction time increasing, new features assigned to monodentate nitrate (1548 cm^{-1}) and gaseous NO$_2$ (1646 cm^{-1}) appeared and strengthened, indicating NO$_x$ began to absorb on surface of sample. The band located at 1360 cm^{-1} is assigned to *cis*-N$_2$O$_2^{2-}$ species in Fig. 6a$_1$. Subsequently, Fig. 6b$_1$- b$_2$ exhibits the *in situ* DRIFTS spectra in reversed pre-adsorption order on C-CZO$_v$. As reaction time was prolonged, the band at 1548 cm^{-1} (monodentate nitrate) slowly decreased (but did not disappear within 20 min) after the introduction of NH$_3$, and the feature at 1360 cm^{-1} (N$_2$O$_2^{2-}$ species) only showed a slight decrease at the same time. The band assigned to gaseous NO$_2$ at 1646 cm^{-1} was basically retained. Thereafter, the new band ascribed to NH$_3$ coordinated to L-acid site (1159, 1223 cm^{-1}) also appeared because of NH$_3$ absorption. These facts indicate that the absorbed NH$_3$ mainly react with gaseous NO by E-R mechanism. The adsorbed NH$_3$ species reacted with gaseous NO to form active intermediate NH$_2$NO/NH$_3$NO over C-CZO$_v$, and then decomposed to N$_2$ and H$_2$O. [45] To some extent, the E-R mechanism alleviates the deactivation of catalyst caused by the competitive adsorption between NO$_x$ and SO$_2$, contributing to the excellent SO$_2$-toletance of C-CZO$_v$.

The transient reactions over CZO were investigated as well (Fig. 6c$_1$, c$_2$, d$_1$, d$_2$). After the pretreatment with NH$_3$, the sample surface was covered by diverse NH$_3$ adsorbed species in Fig. 6c$_1$-c$_2$, containing NH$_4^+$ (1389 cm^{-1}) bonded to B-acid sites and the coordinated NH$_3$ combined with L-acid sites (1218 cm^{-1} and 1567 cm^{-1}). When switching to NO+O$_2$, the signal of all the pre-absorbed NH$_3$ bands exhausted within 2 min, and some features of nitrate species (1545 cm^{-1} for monodentate nitrate, 1429 cm^{-1} for linear nitrite and 1226 cm^{-1} for bidentate nitrate) appeared. [13] Especially, the linear nitrite was oxidized to nitrate as time went on. Then, the *in situ* DRIFTS of reactions between NH$_3$ and pre-adsorbed NO$_x$ species were also collected (Fig. 6d$_1$-d$_2$). It can be clearly seen that the intensity of bridged nitrate (1609 cm^{-1}) and monodentate nitrate (1535 cm^{-1}) bands decreased progressively within 20 min after NH$_3$ was injected to the IR chamber. However, there was less change about bidentate nitrate (1218 cm^{-1}), indicating that bidentate nitrate on CZO was less reactive. In addition, the NH$_3$ adsorption species (1570 cm^{-1}) slowly formed and enhanced. On the basis of these discussions, it can come to a conclusion that L-H mechanism exists in the NH$_3$-SCR reaction system of CZO at 300 °C. [46] When CZO was exposed to feed gas, NH$_3$ and NO$_x$ were immediately adsorbed to the catalyst surface with the formation of NH$_4$NO$_3$, then NH$_4$NO$_3$ decomposed into the N$_2$ and H$_2$O. Besides, NH$_4$NO$_3$ also could follow the reaction equation (NH$_4$NO$_3$ + NO → NO$_2$ + N$_2$ + 2 H$_2$O), and the NO$_2$ product continued to be adsorbed. [40] Comparing Fig. 6a$_1$-a$_2$ and Fig. 6c$_1$-c$_2$, it can be found that the C-CZO$_v$ delivered a faster consumption rate of absorbed NH$_3$ in comparison with CZO. It suggests that the NH$_3$ activation ability of C-CZO$_v$ is stronger than that of CZO again, and demonstrates that NH$_3$-SCR reaction on C-CZO$_v$ is easier to occur than CZO.

As above-mentioned, the NH$_3$-SCR reaction on C-CZO$_v$ and CZO mainly followed E-R and L-H mechanism, respectively. On the basis of the previous adsorption/desorption capability studies, the existence of surface oxygen vacancies and subsurface oxygen substitutions in C-CZO$_v$ are considered to be critical factors for the E-R mechanism. The doped carbon of C-CZO$_v$ induced the formation of unstable nitrate, the unstable nitrate could be decomposed to NO$_2$ at 300 °C. Finally, the NO$_2$ was reduced to NO by oxygen vacancy to react with adsorbed NH$_3$. However, for CZO, the similar process could not happen due to the lack of subsurface oxygen substitutions and less oxygen vacancy, resulting in the L-H mechanism.

4. Conclusion

In summary, we established a novel carbon-doped CeZrO$_{2-x}$ with dual defects, in which O atoms are substituted by C atoms to generate surface oxygen vacancies and subsurface oxygen substitutions, and applied the catalyst to the removal of NO$_x$. Compared with CeZrO$_x$ prepared by directly mixing metal salts, the carbon-doped CeZrO$_{2-x}$ delivered a broader work window of 250–400 °C with NO$_x$ conversion above 85% and good N$_2$ selectivity. More than that, superior SO$_2$/H$_2$O durability and excellent thermal stability were also displayed at 300 °C. The analysis of H$_2$-TPR, NH$_3$-TPD and *in situ* DRIFTS spectra demonstrated that the surface oxygen vacancy and subsurface oxygen substitution caused by C doping induced the excellent redox properties and superior NH$_3$ adsorption and activation capacity of C-CZO$_v$, resulting in the extraordinary SCR performance. The mechanism investigation revealed that E-R mechanism was dominant in the NH$_3$-SCR reaction process of C-CZO$_v$, while the reaction over CZO followed L-H mechanism. According to the adsorption analysis of NO+O$_2$, it is believed that the different mechanisms are derived from the existence of surface oxygen vacancies and subsurface oxygen substitutions in C-CZO$_v$. In addition, the SO$_2$ +O$_2$-TPD, NH$_3$ +SO$_2$ +O$_2$-TPD and XPS discussion proved that the formation of more zirconium sulfate protected the active component cerium for C-CZO$_v$, and the decomposition of unstable ammonium sulfate released the covered active sites, leading to the less deactivation effect than CZO during SO$_2$-resistance test.

CRediT authorship contribution statement

Ruihua Wang: Investigation, Writing – original draft, Formal analysis; **Zhifei Hao**: Investigation, Writing – review & editing; **Xu Huang**: Partial activity tests; **Yue Peng**: Supervision; **Guoquan Liu**: Investigation; **Yuguo Xia**: Investigation; **Sihui Zhan**: Supervision, Funding acquisition, Writing – review & editing.

Declaration of competing interest

The authors declare that they have no known competing financial interests or personal relationships that could have appeared to influence the work reported in this paper.

Data availability

Data will be made available on request.

Acknowledgements

Appendix A. Supporting information

Supplementary data associated with this article can be found in the online version at doi:10.1016/j.apcatb.2023.123098.

References

[1] Y. Li, T. Chen, S. Zhao, P. Wu, Y. Chong, A. Li, Y. Zhao, G. Chen, X. Jin, Y. Qiu, D. Ye, Engineering cobalt oxide with coexisting cobalt defects and oxygen vacancies for enhanced catalytic oxidation of toluene, ACS Catal. 12 (2022) 4906–4917.

[2] Y. Xu, X. Wang, D. Yang, Z. Tang, M. Cao, H. Hu, L. Wu, L. Liu, J. McLeod, H. Lin, Y. Li, Y. Lifshitz, T. Sham, Q. Zhang, Stabilizing oxygen vacancies in ZrO$_2$ by Ga$_2$O$_3$ boosts the direct dehydrogenation of light alkanes, ACS Catal. 11 (2021) 10159–10169.

[3] W. Hong, Y. Liu, T. Zhu, H. Wang, Y. Sun, F. Shen, X. Li, Promoting the catalytic ozonation of toluene by introducing SO$_4^{2-}$ into the alpha-MnO$_2$/ZSM-5 catalyst to tune both oxygen vacancies and acid sites, Environ. Sci. Technol. 56 (2022) 15695–15704.

[4] Z. Wang, Z. Huang, J. Brosnahan, S. Zhang, Y. Guo, Y. Guo, L. Wang, Y. Wang, W. Zhan, Ru/CeO$_2$ catalyst with optimized CeO$_2$ support morphology and surface facets for propane combustion, Environ. Sci. Technol. 53 (2019) 5349–5358.

[5] K. Chen, T. Jiang, T. Liu, J. Yu, S. Zhou, A. Ali, S. Wang, Y. Liu, L. Zhu, X. Xu, Zn dopants synergistic oxygen vacancy boosts ultrathin CoO layer for CO$_2$ photoreduction, Adv. Funct. Mater. 32 (2022) 2109336.

[6] E. Pastor, M. Sachs, S. Selim, J.R. Durrant, A.A. Bakulin, A. Walsh, Electronic defects in metal oxide photocatalysts, Nat. Rev. Mater. 7 (2022) 503–521.

[7] M. Nolan, S. Parker, G. Watson, The electronic structure of oxygen vacancy defects at the low index surfaces of ceria, Surf. Sci. 595 (2005) 223–232.

[8] M. Nolan, S. Parker, G. Watson, Reduction of NO$_2$ on ceria surfaces, J. Phys. Chem. B 110 (2006) 2256–2262.

[9] S. Xiong, J. Chen, H. Liu, X. Chen, W. Si, Z. Gong, Y. Peng, J. Li, Like cures like: detoxification effect between alkali metals and sulfur over the V$_2$O$_5$/TiO$_2$ deNOx catalyst, Environ. Sci. Technol. 56 (2022) 3739–3747.

[10] W. Tan, A. Liu, S. Xie, Y. Yan, T.E. Shaw, Y. Pu, K. Guo, L. Li, S. Yu, F. Gao, F. Liu, L. Dong, Ce–Si mixed oxide: a high sulfur resistant catalyst in the NH$_3$–SCR reaction through the mechanism-enhanced process, Environ. Sci. Technol. 55 (2021) 4017–4026.

[11] L. Han, M. Gao, C. Feng, L. Shi, D. Zhang, Fe$_2$O$_3$-CeO$_2$@Al$_2$O$_3$ Nanoarrays on Al-mesh as SO$_2$-tolerant monolith catalysts for NOx reduction by NH$_3$, Environ. Sci. Technol. 53 (2019) 5946–5956.

[12] Y. Wang, W. Yi, J. Yu, J. Zeng, H. Chang, Novel methods for assessing the SO$_2$ poisoning effect and thermal regeneration possibility of MOx-WO$_3$/TiO$_2$ (M = Fe, Mn, Cu, and V) catalysts for NH$_3$-SCR, Environ. Sci. Technol. 54 (2020) 12612–12620.

[13] Q.I. Fu, S. Wang, T. Wang, D. Xing, X. Yue, M. Wang, S. Wang, Insights into the promotion mechanism of ceria-zirconia solid solution to ethane combustion over Pt-based catalysts, J. Catal. 405 (2022) 129–139.

[14] E. Mamontov, T. Egami, R. Brezny, M. Koranne, S. Tyagi, Lattice defects and oxygen storage capacity of nanocrystalline ceria and ceria-zirconia, J. Phys. Chem. B 104 (2000) 11110–11116.

[15] J. Liu, Z. Zhao, C. Xu, J. Liu, Structure, synthesis, and catalytic properties of nanosize cerium-zirconium-based solid solutions in environmental catalysis, Chin. J. Catal. 40 (2019) 1438–1487.

[16] K. Wang, Y. Li, L. Xie, X. Li, J. Li, Construction and application of base-stable MOFs: a critical review, Chem. Soc. Rev. 51 (2022) 6417–6441.

[17] F. Bi, X. Zhang, J. Chen, Y. Yang, Y. Wang, Excellent catalytic activity and water resistance of UiO-66-supported highly dispersed Pd nanoparticles for toluene catalytic oxidation, Appl. Catal. B 269 (2020), 118767.

[18] W. Wu, Z. Li, Y. Chen, W. Li, Polydopamine-modified metal-organic framework membrane with enhanced selectivity for carbon capture, Environ. Sci. Technol. 53 (2019) 3764–3772.

[19] Z. Liu, G. Sun, C. Chen, K. Sun, L. Zeng, L. Yang, Y. Chen, W. Wang, B. Liu, Y. Lu, Y. Pan, Y. Liu, C. Liu, Fe-Doped Mn$_3$O$_4$ spinel nanoparticles with highly exposed feoct–O–mntet sites for efficient selective catalytic reduction (SCR) of NO with ammonia at low temperatures, ACS Catal. 10 (2020) 6803–6809.

[20] Q. Wang, W. Sun, T. Xie, L. Cao, J. Yang, Metal-organic framework (MOF) template based efficient Pt/ZrO$_2$@C catalysts for selective catalytic reduction of H$_2$ below 90 °C, Chem. Asian J. 14 (2019) 416–421.

[21] B. Lei, W. Cui, P. Chen, L. Chen, J. Li, F. Dong, C–doping induced oxygen-vacancy in WO$_3$ nanosheets for CO$_2$ activation and photoreduction, ACS Catal. 12 (2022) 9670–9678.

[22] S. Chen, Y. Zhou, Z. Hu, F. Dong, Y. Hu, H. Wang, L. Wang, K. Ostrikov, Z. Wu, Single-atom Ru-implanted metal-organic framework/MnO$_2$ for the highly selective oxidation of NO$_x$ by plasma activation, ACS Catal. 10 (2020) 10185–10196.

[23] S. Gao, X. Chen, H. Wang, J. Mo, Z. Wu, Y. Liu, X. Weng, Ceria supported on sulfated zirconia as a superacid catalyst for selective catalytic reduction of NO with NH$_3$, J. Colloid Interf. Sci. 394 (2013) 515–521.

[24] Y. Mao, P. Wang, L. Li, Z. Chen, H. Wang, Y. Li, S. Zhan, Unravelling the synergy between oxygen vacancies and oxygen substitution in BiO$_{2-x}$ for efficient molecular oxygen activation, Angew. Chem. Int. Ed. 59 (2020) 3685–3690.

[25] L. Zhang, J. Yu, X. Wang, Oxidation treatment of diesel soot particulate on Ce$_x$Zr$_{1-x}$O$_2$, J. Hazard. Mater. 140 (2007) 205–210.

[26] X. Wang, Y. Liu, W. Yao, Z. Wu, Boosting the low-temperature activity and sulfur tolerance of CeZr$_2$O$_x$ catalysts by antimony addition for the selective catalytic reduction of NO with ammonia, J. Colloid Interf. Sci. 546 (2019) 152–162.

[27] Y. Zeng, Y. Wang, S. Zhang, Q. Zhong, A study on the NH$_3$-SCR performance and reaction mechanism of a cost-effective and environment-friendly black TiO$_2$ catalyst, Phys. Chem. Chem. Phys. 20 (2018) 22744–22752.

[28] F. Lei, Y. Sun, K. Liu, S. Gao, L. Liang, B. Pan, Y. Xie, Oxygen-vacancies confined in ultrathin indium oxide porous sheets for promoted visible-light water splitting, J. Am. Chem. Soc. 136 (2014) 6826–6829.

[29] W. Shan, F. Liu, H. He, X. Shi, C. Zhang, A superior Ce-W-Ti mixed oxide catalyst for the selective catalytic reduction of NO$_x$ with NH$_3$, Appl. Catal. B 115–116 (2012) 100–106.

[30] C. Yan, G. Chen, X. Zhou, J. Sun, C. Lv, Template based engineering of carbon doped Co$_3$O$_4$ hollow nanofibers as anode materials for lithium ion batteries, Adv. Funct. Mater. 26 (2016) 1428–1436.

[31] G. Poungchan, B. Ksapabutr, M. Panapoy, One-step synthesis of flower-like carbon-doped ZrO$_2$ for visible-light-responsive photocatalyst, Mater. Des. 89 (2016) 137–154.

[32] L. Xu, C. Wang, H. Chang, Q. Wu, T. Zhang, J. Li, New insight into SO$_2$ poisoning and regeneration of CeO$_2$-WO$_3$/TiO$_2$ and V$_2$O$_5$-WO$_3$/TiO$_2$ catalysts for low-temperature NH$_3$-SCR, Environ. Sci. Technol. 52 (2018) 7064–7071.

[33] L. Zhang, L. Shi, L. Huang, J. Zhang, R. Gao, D. Zhang, Rational design of high-performance deNOx catalysts based on Mn$_x$Co$_{3-x}$O$_4$ nanocages derived from metal–organic frameworks, ACS Catal. 4 (2014) 1753–1763.

[34] S. Yang, Y. Guo, H. Chang, L. Ma, Y. Peng, Z. Qu, N. Yan, C. Wang, J. Li, Novel effect of SO$_2$ on the SCR reaction over CeO$_2$: mechanism and significance, Appl. Catal. B 136–137 (2013) 19–28.

[35] Z. Pu, Y. Liu, H. Zhou, W. Huang, Y. Zheng, X. Li, Catalytic combustion of lean methane at low temperature over ZrO$_2$-modified Co$_3$O$_4$ catalysts, Appl. Surf. Sci. 422 (2017) 85–93.

[36] L. Zhang, L. Li, Y. Cao, X. Yao, C. Ge, F. Gao, Y. Deng, C. Tang, L. Dong, Getting insight into the influence of SO$_2$ on TiO$_2$/CeO$_2$ for the selective catalytic reduction of NO by NH$_3$, Appl. Catal. B 165 (2015) 589–598.

[37] R. You, Y. Zhang, D. Liu, M. Meng, L. Zheng, J. Zhang, T. Hu, YCeZrO ternary oxide solid solution supported nonplatinic lean-burn NO$_x$ trap catalysts using LaCoO$_3$ perovskite as active phase, J. Phys. Chem. C 118 (2014) 25403–25420.

[38] Y. Zheng, S. Thampy, N. Ashburn, S. Dillon, L. Wang, Y. Jangjou, K. Tan, F. Kong, Y. Nie, M. Kim, W. Epling, Y. Chabal, J. Hsu, K. Cho, Stable and active oxidation catalysis by cooperative lattice oxygen redox on SmMn$_2$O$_5$ mullite surface, J. Am. Chem. Soc. 141 (2019) 10722–10728.

[39] M. Nolan, G. Watson, Reduction of NO$_2$ on ceria surfaces, J. Phys. Chem. B 110 (2006) 2256–2262.

[40] R. Wang, Z. Hao, Y. Li, G. Liu, H. Zhang, H. Wang, Y. Xia, S. Zhan, Relationship between structure and performance of a novel highly dispersed MnO$_x$ on Co-Al layered double oxide for low temperature NH$_3$-SCR, Appl. Catal. B 258 (2019), 117983.

[41] Z. Hao, Z. Shen, Y. Li, H. Wang, L. Zheng, R. Wang, G. Liu, S. Zhan, The role of alkali metal in α-MnO$_2$ catalyzed ammonia-selective catalysis, Angew. Chem. Int. Ed. 58 (2019) 6351–6356.

[42] F. Liu, K. Asakura, H. He, W. Shan, X. Shi, C. Zhang, Influence of sulfation on iron titanate catalyst for the selective catalytic reduction of NO$_x$ with NH$_3$, Appl. Catal. B 103 (2011) 369–377.

[43] L. Kang, L. Han, J. He, H. Li, T. Yan, G. Chen, J. Zhang, L. Shi, D. Zhang, Improved NO$_x$ reduction in the presence of SO$_2$ by using Fe$_2$O$_3$-Promoted halloysite-supported CeO$_2$-WO$_3$ catalysts, Environ. Sci. Technol. 53 (2019) 938–945.

[44] L. Zhang, J. Pierce, V. Leung, D. Wang, W. Epling, Characterization of ceria's interaction with NO$_x$ and NH$_3$, J. Phys. Chem. C 117 (2013) 8282–8289.

[45] M. Cheng, M. Jiang, S. Yao, J. Han, S. Zhao, X. Tang, J. Zhang, T. Wang, Mechanism of NH$_3$ selective catalytic reduction reaction for NO$_x$ removal from diesel engine exhaust and hydrothermal stability of Cu–Mn/Zeolite catalysts, J. Phys. Chem. C 122 (2017) 455–464.

[46] L. Han, S. Cai, M. Gao, J. Hasegawa, P. Wang, J. Zhang, L. Shi, D. Zhang, Selective catalytic reduction of NO$_x$ with NH$_3$ by using novel catalysts: state of the art and future prospects, Chem. Rev. 119 (2019) 10916–10976.